

WIND TUNNEL FLUTTER TESTING ON A HIGHLY FLEXIBLE WING FOR AEROELASTIC VALIDATION IN THE TRANSONIC REGIME WITHIN THE HMAE1 PROJECT

Yves Govers¹, Holger Mai¹, Juergen Arnold¹, Johannes K.S. Dillinger¹, Allan K.A. Pereira², Carlos Breviglieri Jr.², Edgard K. Takara², Manoela S. Correa², Olympio A.F. Mello², Rodrigo F.A. Marques², Evert G.M. Geurts³, Ralf J.C. Creemers³, Huub S. Timmermans³, Remco Habing^{4,3}, Kees Kapteijn⁴

¹ German Aerospace Center (DLR)
Institute of Aeroelasticity, 37073 Goettingen, Germany
yves.govers@dlr.de

² Embraer S.A.
São José dos Campos, Brazil
allan.pereira@embraer.com.br

³ Netherlands Aerospace Centre (NLR)
Amsterdam, Netherlands
evert.geurts@nlr.nl

⁴ German-Dutch Wind Tunnels (DNW)
Amsterdam, Netherlands
kees.kapteijn@dnw.aero

Keywords: wind tunnel testing, highly flexible wing, flutter stability.

Abstract: The aircraft manufacturer Embraer, the German Aerospace Center (DLR), the Netherlands Aerospace Centre (NLR) and German–Dutch Wind Tunnels (DNW) have tested an innovative highly flexible wing within an aeroelastic wind tunnel experiment in the transonic regime.

The HMAE1 project was initiated by Embraer to test its numerical predictions for wing flutter under excessive wing deformations in the transonic regime. A highly elastic fiberglass wing-body pylon nacelle wind tunnel model (see Figure 1), which is able to deform extensively, was constructed for the experiment. The model was instrumented with a large number of pressure orifices, strain gauges, stereo pattern recognition (SPR) markers and accelerometers. The wing was tested from $Ma = 0.4$ to $Ma = 0.9$ for different angles of attack and stagnation pressures. The static and dynamic behavior of the wing model was monitored and a new method to analyze its eigenfrequencies and damping ratios was used. In the past, the large amounts of data acquired during such experiments could only be evaluated with a time lag. An efficient method developed by DLR now allows performing the data analysis in real time [1, 2]. As a result, it was possible during the test to identify exactly which safety margins remained before the onset of flutter and the resulting possible destruction of the model.

1 INTRODUCTION

Modern wing structures design is optimized with increasingly light structural elements restricted by performance and safety criteria. High aspect-ratio wings designs improve the aerodynamic efficiency which enables reduced fuel consumption as well as improved mission range. Such designs result in the reduction of structural modes frequencies due to increase in the structure flexibility. Hence, aeronautical structures are more susceptible to excitations which may be aggravated by flutter. The current experiment investigates the non-linear behavior of a high-aspect ratio wing subjected to particular flight conditions. Such conditions result in large structural displacements which affect the wing bending and twist orientation significantly. The capability to both predict and design a wing to accommodate safely such displacements is of great importance to modern aircraft design. Moreover, non-linear aerodynamic interactions with the structure are considered and measured, as well as relevant loads and moments.

The Brazilian aircraft manufacturer Embraer initiated the HMAE1 project to test its numerical predictions for wing flutter and to make future flutter analysis more efficient. The DLR Institute of Aeroelasticity in Goettingen and NLR have been responsible for the pre-design of the wind tunnel model using the methods of aeroelastic tailoring in order to meet the requirements for wing tip deflection and frequency ranges. NLR performed the detailed design of the fiberglass wing including the wing-pylon connection and manufactured the structure with the model's built-in measurement technology.

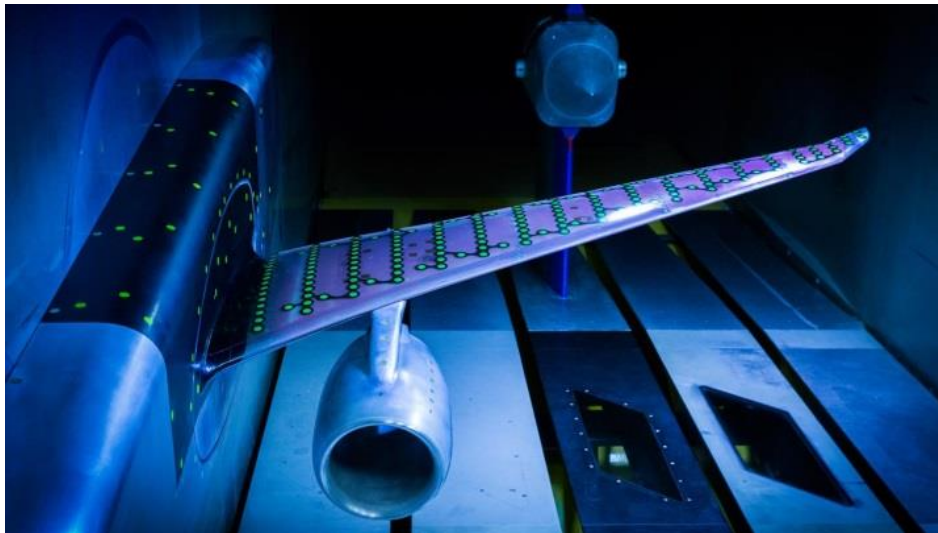


Figure 1: HMAE1 model in HST wind tunnel.

DNW was predominantly responsible for test preparation and test execution. The actual wind tunnel test was carried out at DNW's High-Speed Tunnel (HST) in Amsterdam, using the NLR designed and manufactured wind tunnel model (see Figure 1), with DLR monitoring the loads and conducting the data analysis in real time.

The paper will summarize the ambitious HMAE1 project from the design phase to the wind tunnel test campaign and the data analysis.

2 DESIGN AND MANUFACTURING OF WIND TUNNEL MODEL

2.1 Pre-design

In order to gain insight into the flexibility accomplishable with the projected wind tunnel model, a pre-design study was performed. To this end, an aeroelastic stiffness optimization process developed at the DLR – Institute of Aeroelasticity (DLR-AE) was adopted, with the outcome serving as a starting point for further, more detailed modelling tasks. A detailed description of the process can be found in [3].

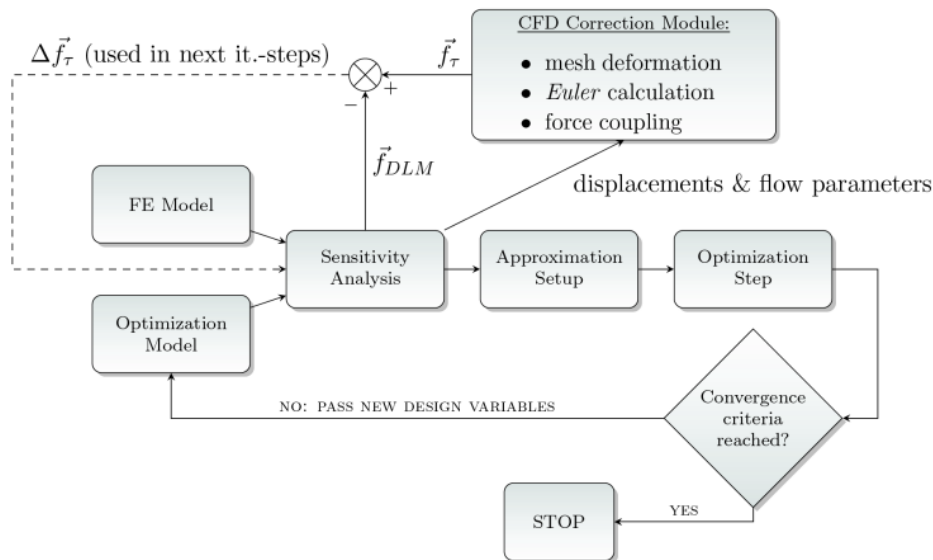


Figure 2: Static aeroelastic optimization framework

The optimization problem is split in two consecutive parts. One, a gradient based stiffness optimization featuring lamination parameter, and two, a stacking sequence optimization based on the results achieved in step one. Both steps rely on a Nastran finite element (FE) model generated with the parametric DLR-AE in-house tool Modgen, [4].

The first optimization part, Figure 2, consists of a successive convex sub-problem iteration procedure, in which a gradient based optimizer consecutively solves a local approximation problem. Responses are approximated as a linear and/or reciprocal function of the laminate membrane and bending stiffness matrices \mathbf{A} and \mathbf{D} . Together with the laminate thicknesses h , they constitute the design variables in the optimization process. Inside the optimization algorithm, stiffness matrices are parameterized by means of lamination parameters, resulting in a reduction in the amount of design variables. The response sensitivities with respect to the design variables are generated with the FE solver Nastran. The stacking sequence design tool, step two in the optimization process, consists of a stacking sequence table (SST)-based genetic algorithm (GA) for the design of blended structures, combined with a modified Shepard's method for improving approximation accuracy in the GA. Details on the optimization strategy can be found in [5]. Both optimization steps feature a CFD correction module that can be applied in order to rectify the doublet lattice method (DLM) aeroelastic loads computed in Nastran, [6].

The wind tunnel model was designed with load carrying skins and a foam core as internal structure, supporting the skins and thus preventing buckling under compression loads. The analysis model is depicted in Figure 3 (left).

The structural responses considered in the stiffness optimization were strain failure in the wing skins, mass and eigenfrequencies, as well as the aeroelastic responses displacement and twist at various span locations. A maximization of the tip deflection for a specific load case was defined as optimization objective. The distribution of design fields - each of which comprises its own set of \mathbf{A} , \mathbf{D} , h variables – within the wing skins, determined the variable stiffness resolution. Various design field distributions were investigated, showing that the application of a single field in chordwise direction provided nearly the same performance in terms of maximum tip deflection as the more construction-elaborate distributions with more design fields. The final distribution is shown in Figure 3 (right).

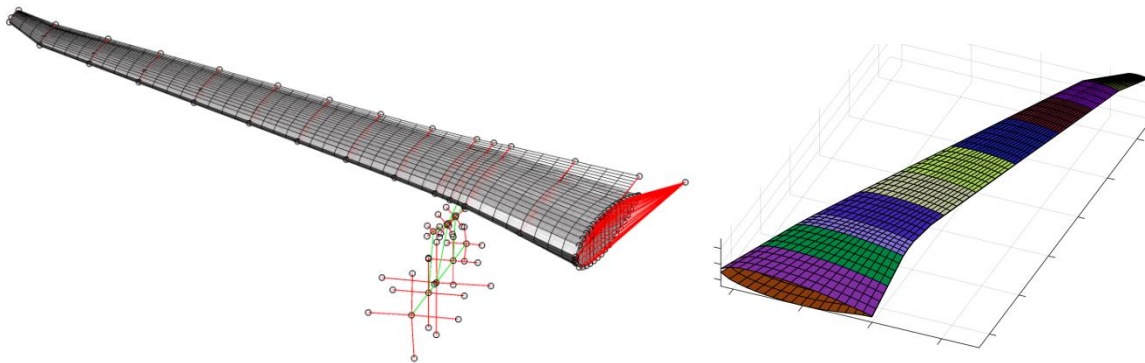


Figure 3: Finite element model (left) and design fields (right)

As to be expected, the optimized maximum tip deflections strongly depended on the strain allowables defined as an input to the optimizer. Moreover, a noticeable degradation of the maximum tip deflection resulted between the theoretically optimal stiffness distribution of optimization step one and the fully blended stacking sequence optimization including manufacturing constraints and a finite number of laminate layers in step two.

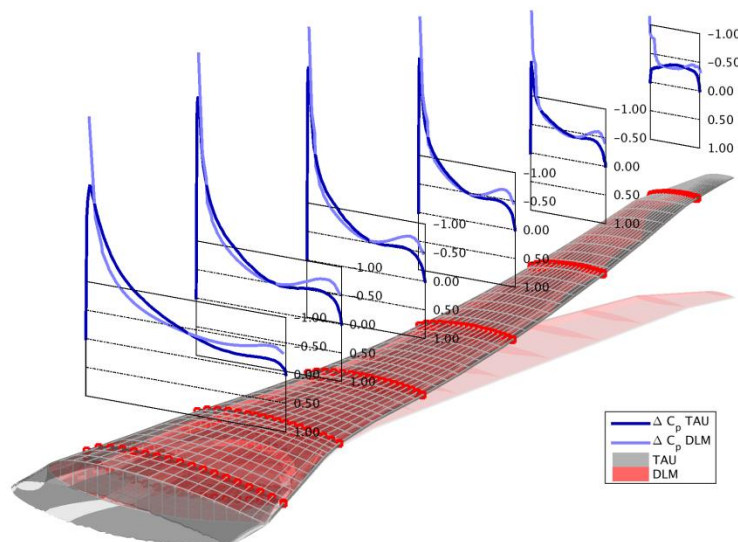


Figure 4: Wing deformation and aeroelastic loading

The deflected wing along with a comparison of the pressure coefficient distributions of DLM and the TAU-Euler CFD computations used for correction are depicted in Figure 4. The outcome of the pre-design optimization served as an input to the detailed design, described in more detail in section 2.2.

2.2 Final design

2.2.1 Structural lay-out

Figure 14 shows a picture of the fully assembled wing. The load-carrying structure of the final wing design is built from a foam core with composite outer skins. To enable high deflections that are required for this wing the skins are made of Glass Fiber Reinforced Plastic (GFRP) materials; glass fibers exhibit linear behavior up to very high strain levels. The lay-up in each of the different sections of the wing has been determined in the preliminary design phase described in section 2.1. In the detailed design phase, these lay-ups were finalized, all individual ply drops were defined and the lay-ups were translated into a manufacturing ply-book. The thickness distribution of both wing skins, obeying manufacturing constraints for build-up/build-down ratios, is shown in Figure 5. The skins are designed such that the strains are close to the maximum allowable strain (including wind tunnel safety factor) in a large area of the wing. Further, unbalanced laminates have been applied. These laminates contain more $+\alpha$ than $-\alpha$ plies, which results in coupling between the bending and torsion modes in the wing. This is called aeroelastic tailoring, which was utilized to obtain the desired frequencies, mode shapes and damping behavior.

To enable the installation of instrumentation (for pressure, strain and acceleration measurements) the wing skin is divided in two parts, an upper skin and a lower skin. The foam core is divided in half over its thickness and in four separate sections in spanwise direction. In the center of the core a groove is cut, which forms the “aorta” to which all the cabling and wiring is routed so that all instrumentation lies in the neutral plane of the wing. This is necessary because the instrumentation cannot withstand the high strains that occur in the skins during the wind tunnel tests. An additional advantage is that the instrumentation will not pick up any load, which makes the stiffness predictions more reliable.

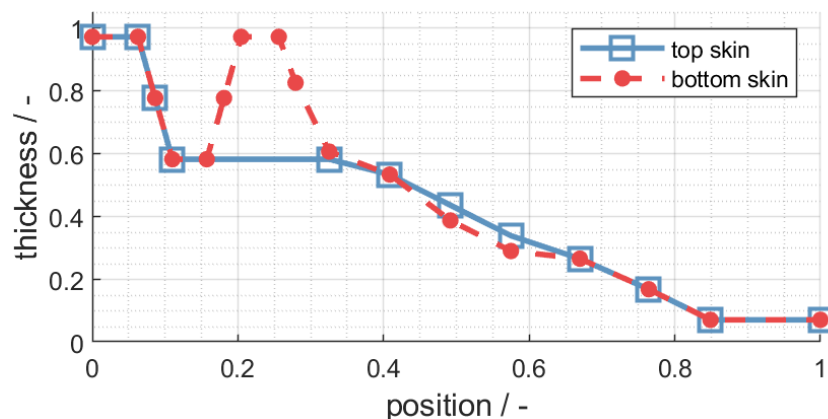


Figure 5: Thickness distribution of the laminate in the top and bottom skin.

Besides the GFRP skins and foam core, the composite wing contains two other major structural elements, the D-spar and the steel adapter at the root. The D-spar consists of the D-spar laminate and the D-spar core, and is divided in three separate sections in spanwise direction to allow for the application of pressure taps in the leading edge. The adapter-to-wing connection consists of both an adhesive joint and an additional bolted connection. The adhesive joint ensures a reliable and well-predictable stiffness of the adapter-to-wing connection up to (at least) the maximum operating load, but the adhesive alone cannot ensure the required safety factor for the wind tunnel. This is what the additional bolted connection is

used for; the bolted connection provides the extra strength (safety factor) that is required for wind tunnel testing.

Finally, the wing contains two metal inserts that are located at the inside of the bottom skin. They are used to enable a bolted pylon-to-skin connection that can be disassembled (for testing without pylon-nacelle). The skin thickness in this area is increased significantly to allow the load transfer from pylon-nacelle into the wing, see the line for the bottom skin in Figure 5.

2.2.2 Computational model and analysis results

A detailed computational Finite Element Model (FEM) of the wing was developed in Abaqus. The model was used for strength and stiffness predictions (a.o. maximum deflections during the wind tunnel test). Further, the detailed Abaqus model was used for extraction of the mass and stiffness matrices in MSC Nastran DMIG format during the preliminary design phase. This MSC Nastran model was used as input for the modal and aeroelastic analyses (including loads and flutter analyses) using MSC Nastran and ZAERO. In a later stage of the project a physical MSC Nastran model was developed which was updated with several ground tests. As the physical MSC Nastran model is used for flutter analyses that are computationally expensive, this model needs to be relatively coarse, see section 3.3. The detailed Abaqus model was used as reference for the (initial) tuning of mass and stiffness in the coarser physical MSC Nastran model.



Figure 6: Abaqus FE-model of the wing.

The detailed Abaqus model is shown in Figure 6 (without the upper skin and upper foam core). The model is an “all solid” model. The skin and D-spar laminates are modelled with continuum shell elements (or solid composites). The foam core, wing tip, pylon-nacelle, and steel adapter are modelled with Tet elements. Cohesive elements are used to model the adhesive interfaces between the different parts. This has been done for all adhesive interfaces except for the interfaces to the foam core. These are modelled with tie constraints because the (thin) adhesive is much stronger and stiffer than the foam. The mass of the adhesive at these interfaces has been included as non-structural areal mass.

Using the MSC Nastran FE model, static and dynamic aeroelastic loads analyses have been done to determine the critical loading inside the test matrix (varying in flow conditions and angle of attack). Dynamic loads analyses included excitation by means of flow turbulence inside the wind tunnel as well as a prescribed pitch excitation, see [7] for more information. The critical loading conditions have been provided to the Abaqus FEM.

The most important analysis results using the critical loading conditions are presented in Figure 7a-c. Figure 7a shows the predicted deformation of the wing for the maximum

deflection load case. The picture clearly demonstrates a strong upward bending deformation for the wing. The maximum displacement is 18% of the semi-span of the wing. This is well beyond the objective of 12-16%. As the goal of the wind tunnel test campaign is to study non-linear effects, it was stated that the higher the deflection the better. This can clearly be achieved with the current design.

Figure 7b and c show the strain distribution in the skin laminates. These are the strains in wing span direction. For upward bending the strains are (of course) compressive in the top skin and tensile in the bottom skin. The maximum compressive and tensile strains can be found outboard of the pylon-nacelle connection, but it can be seen that they are fairly constant in a large area of the wing, especially in the top skin where the laminate does not have to be reinforced for attachment of the pylon. Towards the wing tip the skin laminates become very thin; in the end only a few plies remain. This makes it harder to optimize the strains while still having continuous plies in the laminate, hence the somewhat lower strains towards the wing tip. At the wing root both top and bottom skins are reinforced for attachment to the steel adapter and much lower strains occur as well.

An extensive evaluation of the stresses and strains in all the different components of the wind tunnel model showed that all strength requirements were met. It was concluded that the design is fit for manufacturing, static testing and eventually wind tunnel testing.

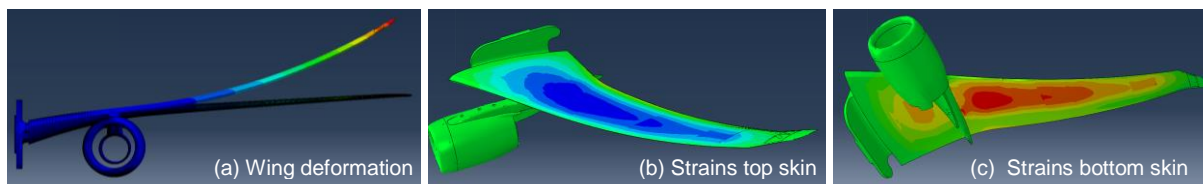


Figure 7: Analysis results for the maximum deflection load case

2.2.3 Modal and aeroelastic analyses

All design phases of the HMAE1 wind tunnel model were accompanied by DLR aeroelastic predictions using tools of different fidelity level to satisfy the physical test boundaries for subsonic and transonic flows. Next to the standard approach based on linear potential-flow theory [7] as provided by the aeroelastic software ZAERO, the approach with fluid structure interaction (FSI) considers all non-linear physics related to large model deformations due to the very flexible design and resulting flow phenomena at transonic speeds. The FSI approach relies on the DLR-AE in-house tool PyCSM [8] which performs the time-accurate coupling of the modal elastic model derived from NASTRAN input and the CFD TAU solver.

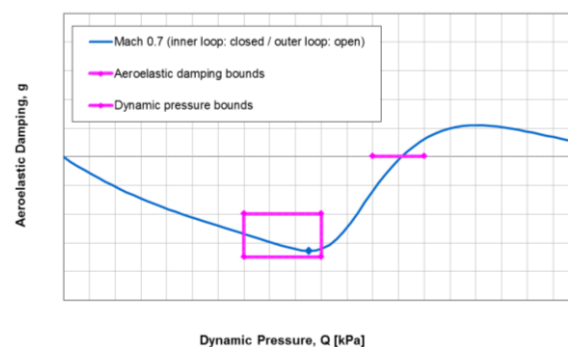


Figure 8: Design bounds for aeroelastic damping of the flutter mode at Mach 0.7

The preliminary and detail design phases considered a test matrix up to a maximum Mach number of 0.7 and according ranges for dynamic pressure and angle-of-attack. Within this matrix, numerous flutter analyses for the assessment of aeroelastic stability were performed to obtain an optimum design of the highly flexible composite wing configuration including substructures for body, pylon and nacelle. The optimized wing structure is tailored to exhibit predefined aeroelastic couplings with major mode contributions from wing bending and engine pitch in the experiment (see Figure 8). Further, the stability assessment included a series of aeroservoelastic analyses to investigate the possible setup of a flutter suppression system by utilizing the model drive train that is available for pitch excitation. According results taking the servo system (see Figure 9) in terms of the transfer functions (TF) for pitch actuator and control loops into account clearly showed the feasibility to suppress the critical flutter mode by introducing a pitch motion in anti-phase within closed-loop mode. For all, the stability behavior and its sensitivity to stiffness and inertia uncertainties of the elastic drive train was assessed with a standard linear potential-flow theory based approach [7], since the initial test campaign inside the DNW HST wind tunnel was constrained to the subsonic speed regime. The underlying structural dynamic models comprise NASTRAN finite element models provided by DLR and NLR as well as experimental modal data from a ground vibration test (GVT) in the test section of DNW-HST measured by DLR. Both approaches consider the dynamic boundary conditions of the wind tunnel setup including the elastic drive train for pitch actuation and the properties of the used piezo electric balance.

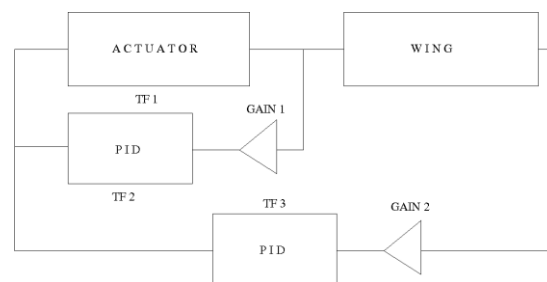


Figure 9: Inner and outer loop of the aeroservoelastic control elements (inner: gain 1 / outer: gain 2)

The second wind tunnel test campaign in the transonic regime for the HMAE1 configuration considered a test matrix up to a maximum Mach number of 0.9 and adjusted ranges for angle-of-attack and dynamic pressure. To assess transonic flow phenomena and to support a safe test entry, fluid structure coupled simulations were prepared to estimate the position and peculiarity of the transonic dip. Due to the shortness of the preparation phase, coupled simulations with PyCSM [8] had to be limited to static aeroelastic cases (see Figure 10), whereas dedicated dynamic aeroelastic stability predictions in time-domain could not be performed before test entry. The static aeroelastic results were evaluated in terms of aerodynamic derivatives to estimate the shape of the transonic dip versus Mach number for several combinations of angle-of-attack and dynamic pressure. Figure 11 gives the result based on the normalized lift slope for a mean angle-of-attack of -2° that indicates the characteristic peak of the transonic dip around the normalized Mach number 0.6. Based on this data, decisions for a safe and efficient wind tunnel operation as well as an emergency shut-down procedure could be drawn before test entry. In parallel, flutter simulations based on DLM aerodynamics as provided by ZAERO were prepared in frequency domain to obtain a rough estimate of the model frequencies and according damping values versus the planned test parameters. Despite knowing that DLM results are physically not correct for transonic speeds, this data was mandatory for the setup of the used real-time online monitoring system (OMA). The underlying structural dynamic model for the PyCSM simulations was the final

NASTRAN finite element model provided by NLR, whilst the experimental modal data measured by DLR was used with ZAERO. As mentioned before, both models consider all the relevant dynamic boundary conditions of the wind tunnel setup.

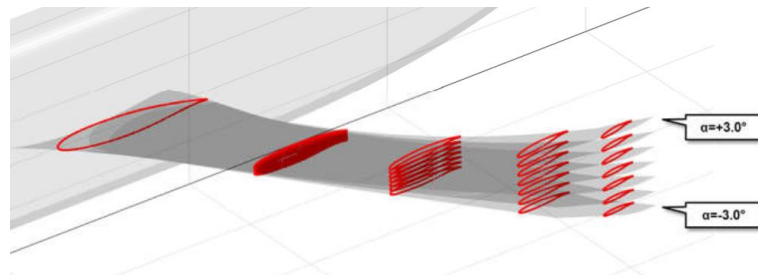


Figure 10: Predicted wing deflections for variation of angle-of-attack from fluid structure interaction

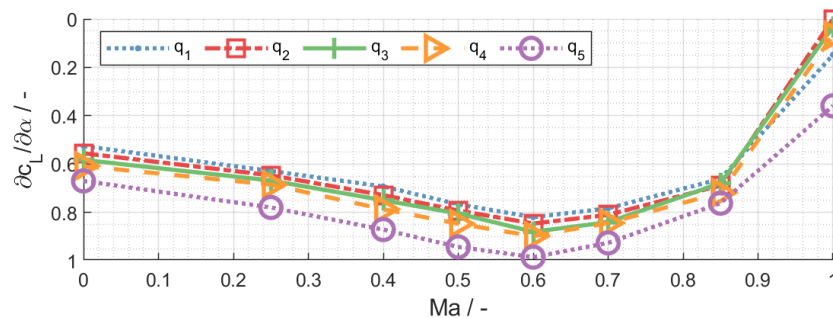


Figure 11: Identification of transonic dip region with lift derivatives for constant angle-of-attack

2.3 Sensor setup

2.3.1 Accelerometers, strain gages, pressure sensors, optical markers

For measuring aerodynamic and aeroelastic features the wind tunnel model was equipped with a large number of sensors including pressure sensors, accelerometers, strain gages and optical markers on the outer skin. Accelerometers were installed in wing and nacelle.

The pressure tubing was mounted on the inside of the wing and routed to the wing root in such a way that extensive bending of the wing cannot damage the tubing.

Strain gage bridges were implemented in the wing to monitor sectional loads during wind tunnel testing. The strain gages were coupled to complete Wheatstone bridges and calibrated during bench testing before the wind tunnel test. The strain gages were bonded to the inner wing skin.

Stereo Pattern Recognition (SPR) markers were dedicated to measure high resolution static deflection. During detailed design it became clear that for a qualitatively good wing bending interpretation, a high number of markers were necessary. The height of the common markers is a disadvantage because they are normally sprayed or glued on the model surface. To overcome this problem to achieve a smooth surface for reliable aerodynamic measurements it was decided to incorporate the markers in the GFRP laminate. Three different solutions were tested for integration of the markers: spray the markers on the laminate, put dots of UV powder on the laminate and using pre-fetched stickers.

The use of stickers gave the best result, which could even be improved by using an additional black ring around the illuminated center. This type of sticker with an additional ring is commercially available. The yellow markers with additional black ring are shown in Figure 1.

Not only the wing but also the fairing contained some SPR markers. Inside the fairing also standard wind tunnel equipment for angle adjustment and verification was installed as were the ESP modules for measuring the static pressures.

2.3.2 Piezo balance

A piezoelectric balance was installed between the model's wing root and the drive shaft. It was used to measure the global steady and unsteady forces and moments acting on the model. During the test it was also possible to monitor the maximum loads.

A piezoelectric balance consists of four piezoelectric elements, each measuring forces in the three directions x , y and z . In the balance coordinate system x and y are oriented in-plane (lift and drag direction) and z in normal direction (side force direction). The four piezoelectric elements are arranged in a square between two massive steel plates. The elements are pre-stressed so that shear forces in x - and y -direction can be measured. Forces in z -direction can be measured by putting or releasing the pressure on the elements.

Piezoelectric elements used in the HMAE1 balance are Kistler Type 9068 and 9067. Each element has a maximum force of ± 20 kN in x - and y -direction and 200 kN in z -direction. As the pre-stress is typically 160 kN the z -range is ± 40 kN. Overload protection is 10% for each direction. The elements have a sensitivity of ~ 8 pC/N in x - and y -direction and ~ 4 pC/N in z -direction. Stiffness of the elements is 700 N/ μm in x - and y -direction and 4500 N/ μm in z -direction.

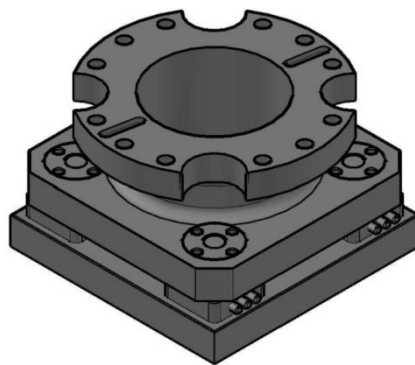


Figure 12: Schematic picture of the piezoelectric balance.

By adding or subtracting the appropriate x -, y - and z -components, three forces and three moments in x -, y - and z -direction and around the x -, y - and z -axis can be calculated. This is done by an 8×6 calibration matrix. Crosstalk of components is taken into account also in the calibration matrix. The coordinate system is right hand, with moments according to force direction. The 8×6 calibration matrix is derived from a systematic loading in all directions and moments. In the laboratory, a calibration matrix for the sensitivities of the eight component channels (X14, X23, Y12, Y34, Z1, Z2, Z3, Z4) was measured. These sensitivities in N/pC are a fixed input to the eight Kistler charge amplifier channels. By this the amplifier does not deliver amplified charges but directly Volts per Newton. The ratio Volts/Newton is defined with the scaling factor and is adapted to the expected maximum forces in the eight

components. In the HMAE1 test the scaling factor was set to 1000 N/V until MP 432 and then increased to 2000N/V for the rest of the test.

Accuracy of the calibration is checked by comparing applied loads and measured/calculated loads: For a maximum absolute value of applied loads of 392.44 N, a maximum deviation of the measure loads from the applied loads of 3.96 N was observed. This corresponds to an accuracy of 1.01% F.S. For a maximum absolute value of applied moments of 202.10 Nm a maximum deviation of the measured moment from applied moments of 0.46 Nm was observed. This corresponds to an accuracy of 0.23% F.S.

2.3.2.1 Correction of balance results

On its static signals, the piezoelectric balance exhibits several time-, temperature- and pressure- dependencies, which affect the signals of a single balance in 3D-configuration as used in the HMAE1 DNW-HST wind-tunnel test.

Internally, each charge amplifier has a time depending drift. This drift results from fault currents and the decay of charges in the amplifier and is strictly linear. It can be corrected by measuring a zero value before and after the test under identical conditions just with the testing time passed by. Linear interpolation to the point in time of the measurement gives the correction value to be subtracted from the measurement value.

The z-components exhibit a drift in temperature. This is not a drift but a linear dependency due to the elongation of the element crystals and the pre-stress bolts. Due to the ring-shape of the elements this is only affecting the z-components but not x and y. This temperature dependency was measured before the wind-tunnel test several times in the laboratory:

- -23.575 N / deg in Z1
- -42.984 N / deg in Z2
- -36.727 N / deg in Z3
- -35.388 N / deg in Z4

Due to a very small enclosed volume between each piezo-element and the pre-stress bolt going through it and due to the very good sealing and high pre-stress forces of the elements, the z-components exhibit also a dependency to changes of the ambient pressure. A correction of the mean static data for this pressure dependency is possible relative to the zero-point for each measuring point. The following correction values were derived:

- 0.0017116 N/Pa in Z1
- 0.0016986 N/Pa in Z2
- 0.0018215 N/Pa in Z3
- 0.0017132 N/Pa in Z4

and applied relative to the zero values of the pressure at zero measurement.

The piezoelectric balance is calibrated to measure forces and moments as cutting forces in the balance-centered coordinate system. When the balance is turned from its zeroed position (usually at $\alpha=0^\circ$), some of the weight force will move into the side-force direction with increasing angle-of-attack. This was measured during the test and derived to:

$$X14 = -3.8754 \text{ N/deg}$$

$$X23 = -4.3123 \text{ N/deg}$$

For the lift the correction is 1.5N/deg. and therefore not taken into account.

The piezoelectric balance always measures normal and tangential forces, not lift or drag. Normal and tangential forces have to be transformed to lift and drag by a sine and cosine function and the angle-of-attack:

$$\text{Lift Force} = \text{Normal Force} * \cos(\alpha) - \text{Tangential Force} * \sin(\alpha)$$

$$\text{Drag Force} = \text{Normal Force} * \sin(\alpha) + \text{Tangential Force} * \cos(\alpha)$$



Figure 13: Piezoelectric balance during load check.

2.3.2.2 Quality of Results

2.3.2.2.1 Accuracy

Load checks were performed before and after the HMAE1 W/T entries. All six forces and moments were tested by applying loads and measuring back the forces and moments. From the comparison of applied and measured values, relative differences were calculated and set in relation to the full range achieved in the test. Applying this procedure, the following range of relative difference could be derived:

Normal Force	-0.80% ... -0.90%
Tangential Force	0.70% ... 1.80%
Side Force	-0.10% ... -2.60%
Yaw Moment	0.30% ... 1.00%
Roll Moment	-0.50% ... -0.70%
Pitch Moment	0.03%

2.3.2.2.2 Repeatability

Test points at $Ma=0.700$ and $p_0=120\text{kPa}$ were repeated for three angles-of-attack (-2, -1 and 0 degrees) to check for the repeatability of the measurements. The relative differences between the results were in the range:

Lift Force	-0.3% ... 0.2%
Drag Force	0.2% ... 2.7%
Pitch Moment	-0.8% ... 0.1%
Side Force	-3.5% ... 8.3%
Yaw Moment	0.0% ... 2.3%
Roll Moment	-0.6% ... -1.1%

2.4 Manufacturing of wind tunnel model

Figure 15 presents a glossary of the different manufacturing steps in the production of the composite wing. The wing skins are made by means of a vacuum injection process. Dry glass fibre plies are laminated in the mould and vacuum pressure is used to inject the resin into the laminate, see Figure 15a and b. The resin is a two-component system that cures at room temperature, which results in high dimensional accuracy as it eliminates any effects due to shrinkage.

After machining of the skins, the instrumentation, including pressure taps, accelerometers and strain gages, is installed at the inside of the skin. The different foam parts are bonded to the skins and the cabling is routed to the aorta and from there to the wing root. At the wing root all the cabling exits the wing near the leading edge just in front of the steel adapter which is shown in Figure 14.



Figure 14: The assembled wing with pylon-nacelle.

In the final step the two wing halves are assembled with the steel adapter and wing tip, see Figure 15c. All parts are joined in a single manufacturing step using dedicated assembly tooling. The wing is finished by installing the double bolt row in the skin and wing root adapter, and by bolting on the pylon-nacelle. The fully assembled wing is shown in Figure 14.

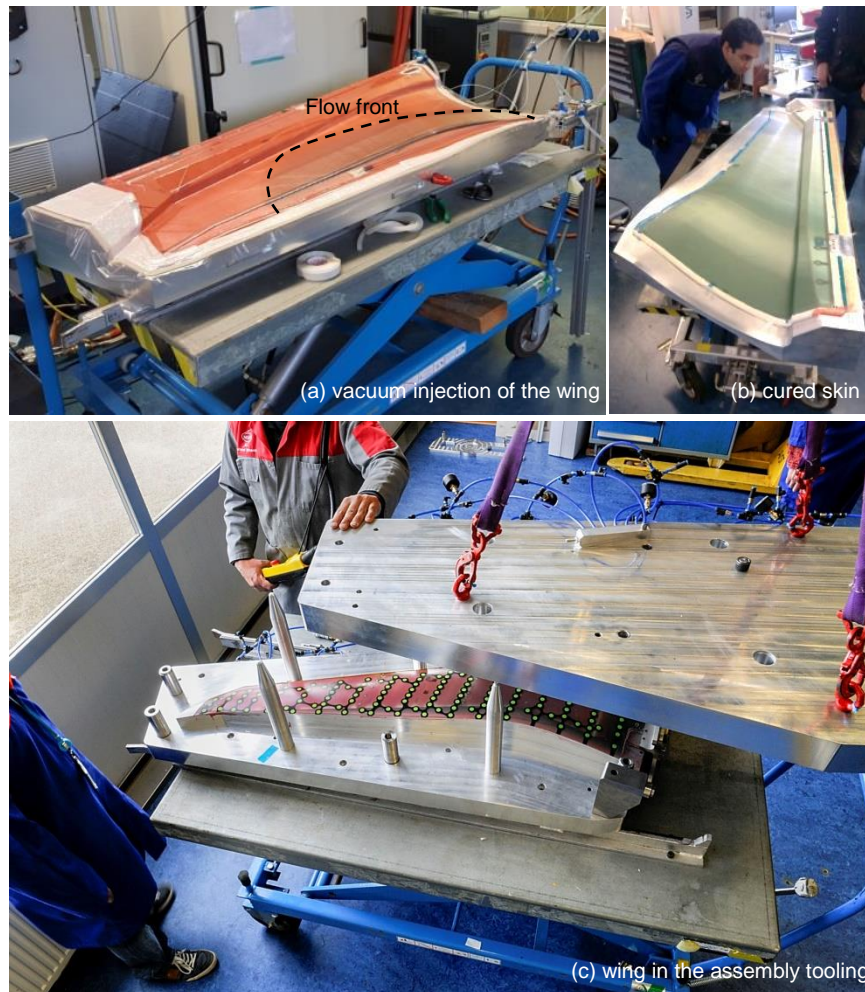


Figure 15: Different steps in the manufacturing process of the wing.

3 PRE-TESTING AND MODEL CALIBRATION

3.1 Static testing

Before entering the wind tunnel a static test has been performed on the wing. The goal of this test was threefold:

1. To validate the strength of the wing up to the design load (including the pylon-to-wing connection and the adhesive joint at the adapter-to-wing connection) and to determine the maximum deflections that will be achieved in the wind tunnel.
2. To calibrate the Wheatstone bridges (strain gauges) in the wing with the applied loads. The strain gauges are used for safety monitoring during the wind tunnel test.
3. To validate the FEM analyses with the detailed Abaqus model (material stiffness properties and modelling method).

The test set-up is shown in Figure 16. As only a few different load cases had to be applied, a practical solution was designed for the test; the wing is positioned upside down and the aero loads on the wing and pylon-nacelle are applied by adding weights. The loads are introduced into the wing via 6 specially manufactured sleeves and the existing motor pylon.

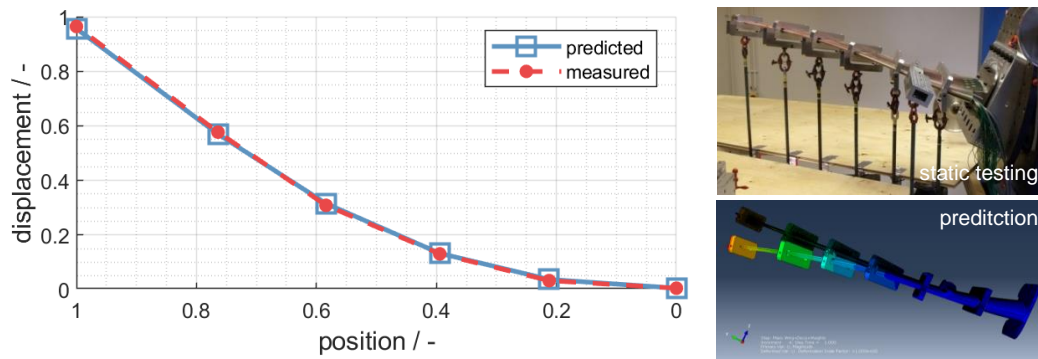


Figure 16: Comparison of displacements from FEM and measurements from static test.

During static testing the wing has been positioned upside down and the displacements were measured at the locations of the 6 sleeves and the motor pylon. Figure 16 shows a comparison of the test results with the FEM analysis. The displacements predicted with the detailed Abaqus model show excellent agreement with the measured displacements. This shows that the stiffness prediction of the wing is very accurate.

3.2 Ground vibration testing (GVT)

Modal testing of the HMAE1 wing was performed with different structural configurations and boundary conditions. Already during the manufacturing process the wing was tested in varying boundary conditions as well as after final assembly in the wind tunnel test section mounted to the wind tunnel wall including the piezo balance.

3.2.1 GVT outside wind tunnel

Before the static testing as described in section 3.1, an initial GVT provided modal data of the manufactured structure for model validation including updates of wing, wing-to-eylon connection and wing-to-balance adapter (thus, without drive-train) to address the first five prescribed mode shapes and frequencies.

The ground vibration tests were performed in a laboratory environment at the calibration facility of DNW-HST. Two different boundary conditions have been tested, clamped (model suspended to a heavy base support structure) and free-free (model suspended in springs) to provide modal data to facilitate model-updating of the structural dynamic FEM (Figure 17).

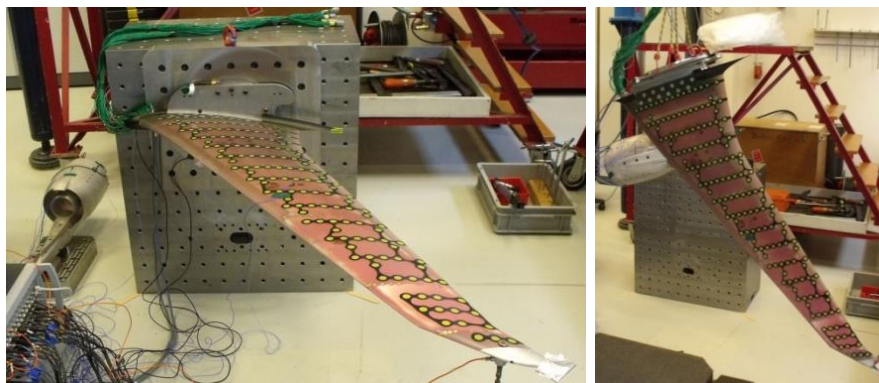


Figure 17: Test set-up for WB in clamped condition (left) and WPBN in free-free condition (right)

After finishing the static load test and calibrations, a second GVT was performed, identical to the first one, to verify the integrity model by comparing the wing's dynamic characteristics after being subjected to the effects of high loads and resulting large displacement. From this GVT it was concluded that no damage was inflicted to the wind tunnel model. A more detailed description of bench testing is presented in [7].

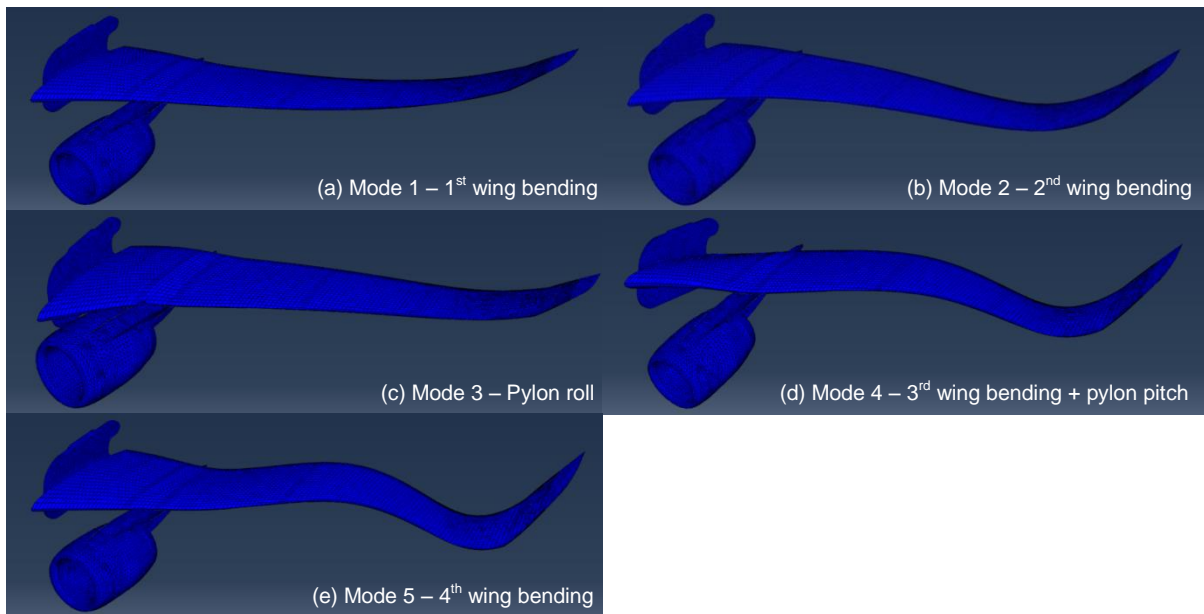


Figure 18: First five mode shapes (free-free conditions) as determined with the detailed Abaqus model.

The GVT tests have been compared with eigenfrequency analyses using the detailed Abaqus model. Figure 18 and Table 1 only show the results for the free-free conditions, but both free-free and clamped conditions have been evaluated. For both test conditions the analysis results are within $\pm 3.5\%$ frequency deviation of the test results for the first five modes. There is a very good agreement between test and analysis, considering that no mass or stiffness tuning has been performed for any of the materials used in the FEM model. Also the stiffness of the pylon-to-wing connection is modelled accurately; this, however, did require a small modification in the way the connection was modelled, which was related to the way the wing was eventually manufactured. It can be concluded that both mass and stiffness distribution are accurately captured by the detailed Abaqus model.

Table 1: Comparison between FEM results and GVT measurements (free-free conditions).

<i>Mode</i>	<i>Description</i>	<i>Error, %</i>
1	1st wing bending	-1.2
2	2nd wing bending	-3.4
3	Pylon roll	+3.5
4	3rd wing bending + pylon pitch	-2.6
5	4th wing bending	-3.2

3.2.2 Modal testing inside test section of wind tunnel

Before wind tunnel entry the dynamic characteristics of the model attached to the wind tunnel wall were determined by experimental modal analysis. Response data from the model in two structural configurations was analyzed, wing body pylon nacelle (WBPN) and wing body (WB) only. Not only structural configurations have been modified but also boundary conditions. Furthermore, tip and nacelle mass variations have been introduced and different sensor setups with internal and external sensors were investigated. Overall, 12 different configurations have been analyzed.

Purpose of the Ground Vibration Test (GVT) was to determine an equivalent modal model including resonance frequencies, mode shapes, generalized masses and damping ratios, to build frequency response functions (FRF's) of the HMAE1 model and its support structure and to gain physical insight in the effect of the operating hydraulic actuator system on the models modal characteristics.

In detail GVT campaign was to

- quantify possible differences between the boundary conditions at the wing root like fixed lever and controlled inner loop “on”,
- clarify the presence of non-linearities with increasing force levels using swept sine excitation with electro dynamic shakers,
- check the correct operation of the internal sensors,
- analyze the effect of variation of tuning masses in wing tip and nacelle,
- provide results that can be used to represent the structural behavior in a flutter analysis,
- provide results that can be used for finite element model updating and
- analyze the possibility to excite the modes of the structure by pulses performed with the hydraulic actuator.

For the GVT internal and external sensors have been used. The structure was excited either with a long coil electrodynamic shaker or by impact hammer. Figure 19 gives an overview of the GVT setup with shaker and external sensors. The test setup presented in Figure 19 has been used to demonstrate that the internal sensors work properly. Furthermore, the non-linear behavior of the whole test setup has been analyzed. Therefore artificial excitations with swept-sine signals on different force levels have been used to check for non-linear structural behavior due to the hydraulic pitch actuator. To capture all modes with high quality four different excitation locations have been used; nacelle in y/z and wing x/z.

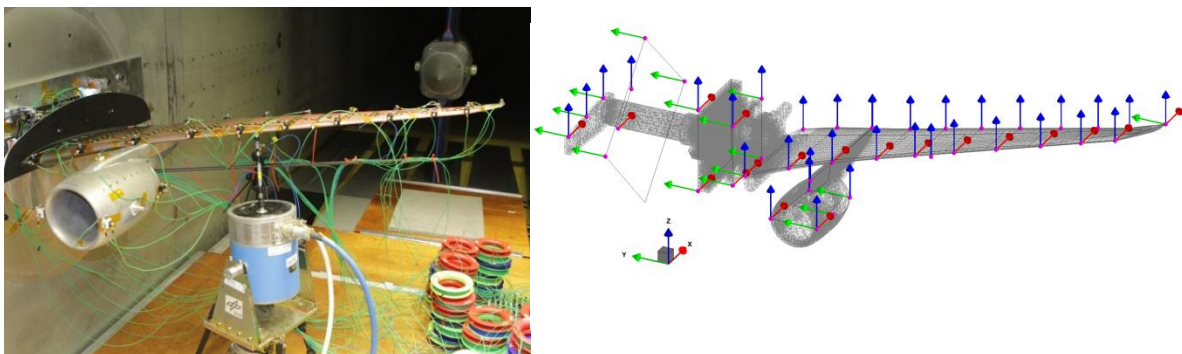


Figure 19: GVT setup in wind tunnel (left) and sensor locations with external accelerometers (right).

The maximum frequency deviation that was detected for an eigenfrequency due to increasing force levels was about 1% which is negligible. Final modal data for model calibration of the wind tunnel test setup was determined from hammer testing with an inverted sensor/exciter location setup as described before.

3.3 Model calibration

Before wind tunnel testing the model is calibrated with data from static and ground vibration testing using computational model updating techniques. As mentioned in Chapter 2.2.2, two different FEM models have been developed during the extent of the HMAE1 project; the Abaqus model used for strength and stiffness predictions and the MSC Nastran model used for loads (static and dynamic) and flutter analyses, see [7]. The later one, the MSC Nastran model, has been updated and correlated up to the final GVT inside the wind tunnel test section to have a high correlation in structural dynamic characteristics with the manufactured model. In the end, the updated MSC Nastran FEM was used for flutter predictions in order to validate the flutter behavior in the entire test with the objectives set by Embraer.

During the detailed design phase it was decided to include a high fidelity representation of the boundary condition (wind tunnel interface parts) in the MSC Nastran structural dynamic FEM. The boundary conditions have a significant effect upon the structural dynamic characteristics of the model and therefore on the aeroelastic flutter behavior. Due to the fact the model was developed to have deterioration of damping for the flutter mechanism inside the test matrix, the numerical FEM, as input to the flutter analyses, was required to be as accurate as possible. Figure 20 shows the full MSC Nastran FEM including the full wing-pylon/nacelle, piezo balance, axle-to-balance adapter, axle itself and lever for pitch control. For more information about the development of the model please refer to [7].

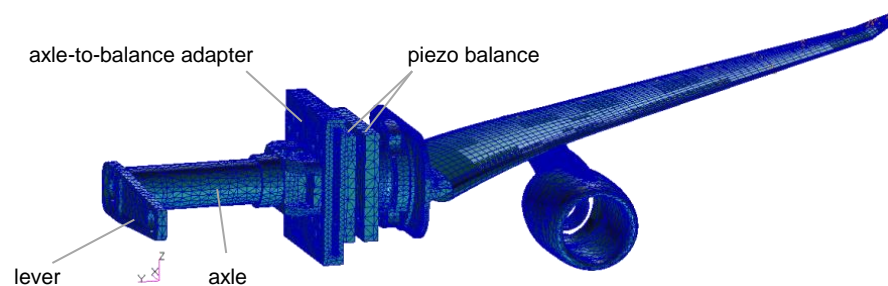


Figure 20: MSC Nastran FEM including the high fidelity boundary conditions (wind tunnel interface parts).

As discussed in Chapter 3.2, various GVT's have been used in order to focus model correlation and updating. The pylon-nacelle and wing have been tested separately to obtain test data which has been used for component updating. After successful adaptation of the individual parts the data from the GVT of the fully assembled WBPN was used to focus on the connection between the lower wing skin and upper pylon. Updates for the wing-to-eylon connection were included in the FEM. After update a high correlation between test and prediction was achieved underlined by high values for the Modal Assurance Criterion (MAC) matrix and low frequency deviations for the first 10 modes. The correlation of the pylon pitch mode between analysis and GVT results performed outside of the wind tunnel (fixed boundary conditions on a support structure) is shown in Figure 21.

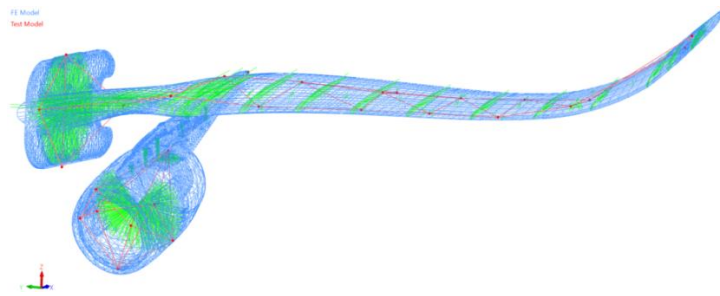


Figure 21: Pylon pitch mode correlation between the MSC Nastran FEM (blue) and test wireframe (red).

In the end, a GVT was performed by DLR inside the wind tunnel (see Figure 19) in order to update the high fidelity drivetrain (the actual boundary condition used during the tests). The final updated FEM including the high fidelity boundary condition showed a high correlation for different configurations tested. Figure 22 shows the high MAC correlation (left) between the full FEM and final GVT results inside the wind tunnel set-up and the correlation of the first mode shape (right).

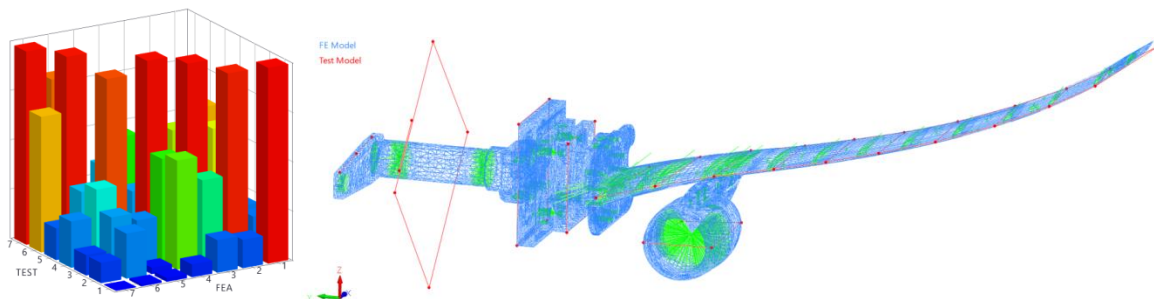


Figure 22: MAC matrix between FEM and wind tunnel GVT (left) and overlay of 1st wing bending (right).

4 WIND TUNNEL TEST SETUP

4.1 Wind Tunnel Facility

The test has been performed in the high-speed wind tunnel HST located in Amsterdam, the Netherlands. The 1.60/1.80 by 2.00 m² HST is a variable density closed circuit wind tunnel. The stagnation pressure can be varied between 25 and 390 kPa. An adjustable nozzle is followed by a test section with solid side walls and movable slotted top and bottom walls. Top and bottom walls can be adjusted to obtain a test section height of 1.60 m or 1.80 m. The present test has been performed in the 1.80 m test section configuration. The test section is calibrated for Mach numbers between 0.2 and 1.30.

4.2 Test and measurement setup

The model has been assembled on the half model support at the test section side wall (see Figure 1). The wing root of the model has been connected via an axle to a dedicated hydraulic actuation system. The model and drive system are connected with a turn table to allow changing the angle of attack. The acquisition of the signals from the various tunnel and model instrumentation has been performed with various subsystems. The steady signals were measured by the standard data acquisition system of HST and dedicated optical systems were triggered by a common signal (e.g. infrared thermography for shock or transition localization and stereo pattern recognition for wing deflection). The unsteady signals were measured by two independent dynamic data acquisition systems i.e. VIPER (DNW, [9]) and Dewetron (DLR) connected to the frontend input of the VIPER.

Following time signals were measured: piezoelectric balance, accelerometers, strain gage bridges, laser distance measurement devices, servo valve control signal. An additional software low-pass filter (-3dB at 1.5 kHz) was applied. In parallel acceleration, strain gage signals, forces from the piezo balance and wind tunnel parameters have been acquired by DLR's Dewetron measurement system for dedicated online processing to assess the flutter stability online.

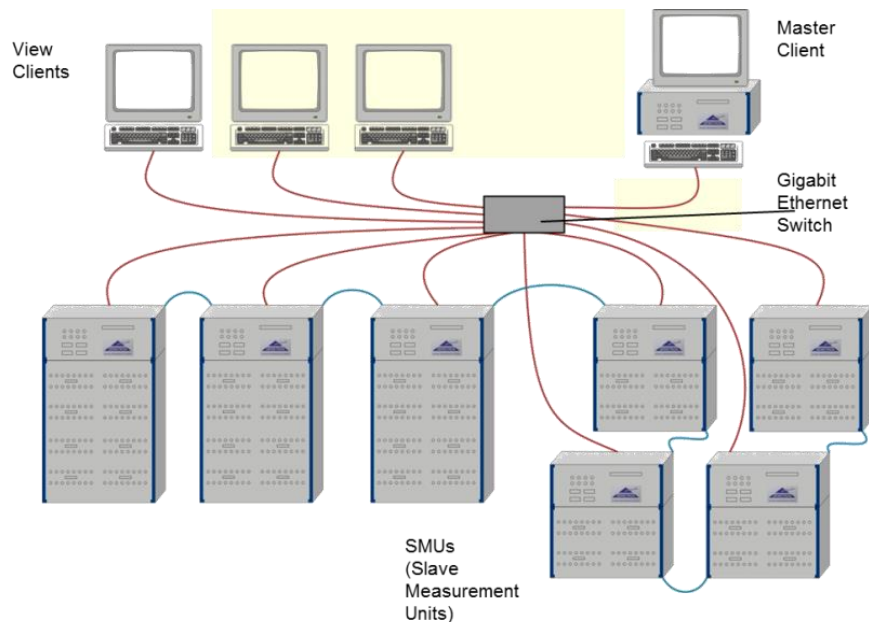


Figure 23: DLR AMIS III data acquisition system.

The data acquisition system for unsteady signals AMIS III of DLR is a modular system of about 1000 channels. The channels are grouped in subsystems of 16, 64 and 128 channels in one frontend. The frontends can be used individually as single systems or grouped to one large system with 1000 channels. All channels are sampled fully synchronized with a sample rate of 204.8 kHz per channel. Each channel consists of an analogue input module for signal conditioning and a 24bit sigma-delta analogue-digital converter. As data can be written directly to the hard drive recording time is online limited by the disc space. Data can be recorded on one master system and viewed or processed as online data on several view client systems. Furthermore data can be received by other computers via an ActiveX interface.

4.3 Control room setup

In order to enhance the test safety and quality, prior to testing a so-called communication protocol has been defined. This protocol defines responsibility persons of all subsystems, normal operation and error cases.

The test matrix comprises various combinations of Mach numbers (Ma), dynamic pressures (q) and angle of attack (AOA). The measurements at various Ma , q , AOA combinations were only performed as long as the conditions were deemed to be safe. Test safety and model health were judged via

- (a) the assessment of the flutter margin by real-time modal analysis including damping trend prediction and comparison with simulation results, online piezo balance spectrum and time data statistics,

- (b) the monitoring of the model integrity by global loads from piezo balance, sectional loads from strain gages and fouling detection and
- (c) an online video from the test section.

Online graphs of the steady data (e.g. flow conditions, pressure coefficients, piezo balance and a camera image of test section) results and IRT images were displayed on monitors in the HST control room as well.

In combination with the measurement software DEWESOFT online displays have been generated to monitor the overall loads on the model with the balance signals which can be seen in Figure 24 on the right hand side. The data stream from DEWETRON system can also be accessed online via an ActiveX interface. The online data was used to feed DLR's online monitoring software suit to directly estimate eigenfrequencies and damping ratios from operational modal analysis shown in Figure 24 on the left hand side. The modal parameter estimates were plotted over time using an efficient mode tracking algorithm.



Figure 24: Displays in control room: modal parameters (left) and balance signals (right).

Besides eigenvalue and damping estimates Figure 24 also shows balance signals to monitor the overall loads for structural integrity.

4.4 Test matrix

Two test campaigns have been conducted. The wing body configuration was only tested during the first campaign and for static properties only. The wing body pylon nacelle configuration was tested during both test campaigns for static and dynamic properties. The test matrices have been optimized to account for safety and efficiency.

5 WIND TUNNEL TESTING

5.1 Balance monitoring and loads analysis

To ensure model integrity and wind-tunnel safety, the load signals from the piezoelectric balance were monitored online in the control room and in the customer room as shown in Figure 24 on the right hand side. The voltage signals were recorded by the Dewetron DAQ system. The input data was monitored online for the single components of the balance. In addition the calibration matrix was applied within Dewesoft to calculate forces and moments in real time. In a next step the aerodynamic coefficients were calculated online in the data acquisition system. The resulting forces and moments as well as coefficients were displayed on a screen as online data during the test in the control room and in the customer room. Floating mean values and amplitudes of the dynamic data were calculated as new virtual data

channels. Furthermore limits were set inside the software for each channel to supervise maximum loads and display a warning when limits were approached.

Additionally sectional loads from strain gages have been monitored by DNW. The loads have been calculated offline directly after recording of a test point using the calibration matrix determined before test entry.

5.2 Online frequency and damping estimates

Over the recent years DLR-AE has developed real time modal analysis capabilities for wind tunnel and flight testing from turbulence excitation only [1, 2, 10]. The analysis methods include operational modal identification algorithms in the frequency and time domain, respectively least squares complex frequency (LSCF, [11]) and stochastic subspace identification (SSI, [12, 13]). During the start of the HMAE1 wind tunnel test campaign, both estimators have been used in parallel. SSI turned out to deliver more reliable and stable damping estimates over time. For this reason SSI was chosen for all further analyses.

Modal identification results for at least the first five modes have been displayed on screen with an update rate of three seconds while the last 60 seconds of time data was analysed. The modal parameters were not only displayed but also tracked over time to see the evolution of frequency and damping curves which was shown on a monitor in the control room (see Figure 24). It is worthwhile to mention that the modal identification and tracking was extraordinarily stable. Therefore the online monitoring provided a good overview of the current stability of the model and served as a reliable basis for a decision to continue to the next test point or to terminate due to aeroelastic stability problems.

Figure 25 gives an overview of the whole process for online monitoring which basically consists of 5 steps. Step 1 is an open data acquisition system that allows grabbing time data blocks in real time with a client PC or sends a data stream to a client PC in step 2. Currently measurement systems from Dewetron, imc, National Instruments, LMS and LUNA are supported. Step 3 incorporates the core of the online monitoring process with the “real” time identification methods. Step 3 delivers the estimates of all modal parameters every two or three seconds, which is performed with the DLR-AE MATLAB toolbox. The output over time is also shown in Figure 26 on the left hand side.



Figure 25: Dataflow of online monitoring process.

Modal data identified in this step is always tracked and directly written to an SQL based multi user access database, step 4. Additionally parameters describing the current state of the wind tunnel or respectively flight state are written to the SQL database.

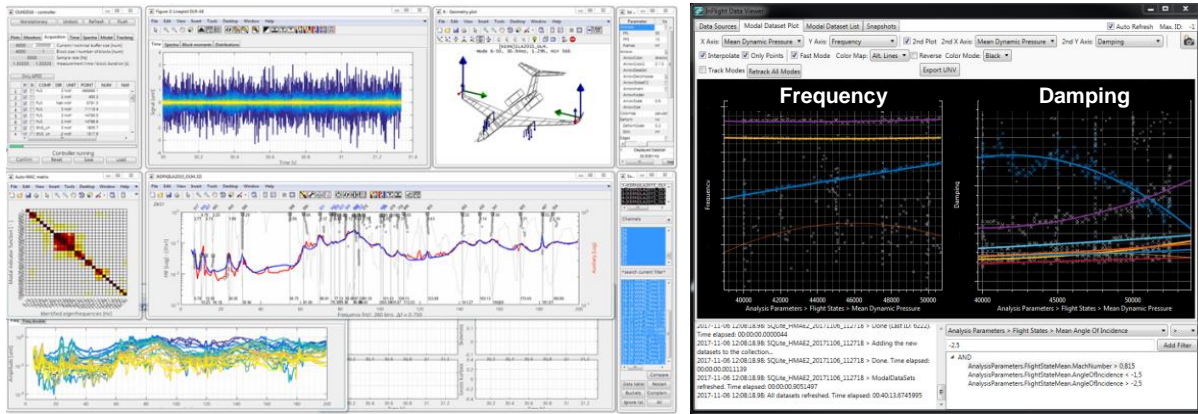


Figure 26: Online modal identification step 3 (left) and step 5 visualization of database (right) with generic data.

Figure 26 (right) shows a view on the database including damping trend prediction, which represents step 5 of the data flow. Especially the blue curve in Figure 26 (right) indicates a rising frequency and a falling damping trend. The data can be visualized with different x, y – plots.

The online monitoring process was running throughout the whole wind tunnel test campaign fully automatically. The provided data guaranteed a safe wind tunnel test operation. Test points close to flutter could be measured while test points beyond the estimated stability boundary due to the identified damping trend were skipped.

6 DATA POST PROCESSING

6.1 Frequency and damping estimates

After the test, all points from the test matrix have been analyzed offline to provide modal parameters for the first five modes. Figure 27 shows a typical plot from offline analysis of the acceleration responses for different test points of the measurement matrix. For offline analysis the SSI algorithm was used again. Figure 27 clearly shows that the identified frequency and damping estimates are meaningful. The challenge was to separate highly and lightly damped modes while eigenfrequencies approached each other.

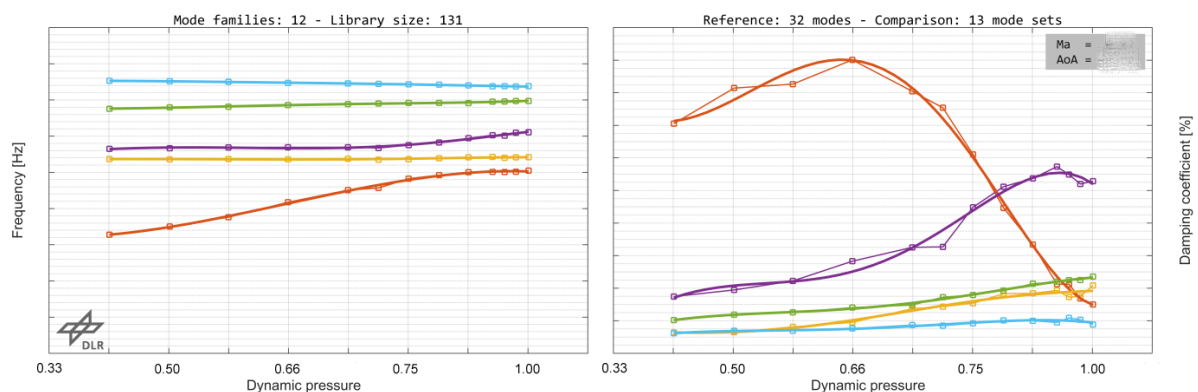


Figure 27: frequency and damping evolution of first 5 modes.

6.2 Balance data

For the processing of the final data from the piezoelectric balance the corrections for time drift, temperature and pressure dependency of the z-components were applied to the balance

raw data. Time series data was corrected and the forces and moments calculated by application of the calibration matrix. Then time series of aerodynamic coefficients were calculated. For a quick look on the data, also mean values were provided from the time series.

7 CONCLUSIONS

The HMAE1 project was very challenging in all its subtasks from model design and model manufacturing over pre-testing and model validation to wind tunnel testing and monitoring as well as the data processing afterwards. Starting from the model design and manufacturing a very complex and highly elastic wind tunnel model has been developed to meet given aeroelastic constraints. Extensive pre-testing for off-wind model calibration has been performed to achieve a representative FE model. During wind tunnel testing full control about the current state of the test was available due to sophisticated monitoring techniques and finally new fields have been opened for flutter testing using just turbulence excitation for the identification of modal parameters to assess the flutter stability. In the end it can be stated that the HMAE1 project was very successful which was based on a good cooperation of all partners NLR, DLR, DNW and Embraer.

8 REFERENCES

- [1] Jelacic, G., Schwochow, J., Govers, Y., Hebler, A. , Böswald, M. (2014). *Real-time assessment of flutter stability based on automated output-only modal analysis*. in International Conference on Noise and Vibration Engineering. KU Leuven, Belgium. pp. 3693-3706.
- [2] Jelacic, G., Schwochow, J., Govers, Y., Sinske, J., Buchbach, R., Springer, J. (2017). *Online Monitoring of Aircraft Modal Parameters during Flight Test based on permanent Output-Only Modal Analysis*, in 58th AIAA/ASCE/AHS/ASC Structures, Structural Dynamics, and Materials Conference, American Institute of Aeronautics and Astronautics.
- [3] Dillinger, J. K. S., Klimmek, T., Abdalla, M. M. , Gürdal, Z. (2013). Stiffness Optimization of Composite Wings with Aeroelastic Constraints. *Journal of Aircraft*, 50(4): pp. 1159-1168.
- [4] Klimmek, T. (2009). *Parameterization of topology and geometry for the multidisciplinary optimization of wing structures*. in CEAS 2009 - European Air and Space Conference. Manchester, UK.
- [5] Meddaikar, Y., Irisarri, F.-X. , Abdalla, M. (2015). *Blended Composite Optimization combining Stacking Sequence Tables and a Modified Shepard's Method*. in 11th World Congress on Structural and Multidisciplinary Optimization. Sydney, Australia.
- [6] Dillinger, J., Abdalla, M. M., Meddaikar, Y. M. , Klimmek, T. (2015). *Static Aeroelastic Stiffness Optimization of a Forward Swept Composite Wing with CFD Corrected Aero Loads*. in International Forum on Aeroelasticity and Structural Dynamics, IFASD 2015.
- [7] Timmermans, H. S., Tongeren, J. H., van, G., E.G.M., Marques, R. F. A., Correa, M. S., Waitz, S. (2019). *Design and validation of a numerical high aspect ratio aeroelastic wind tunnel model (HMAE1)*. in International Forum on Aeroelasticity and Structural Dynamics. Savannah, GA, US.
- [8] Neumann, J. , Mai, H. (2013). Gust response: Simulation of an aeroelastic experiment by a fluid-structure interaction method. *Journal of Fluids and Structures*.

- [9] Holthusen, H. , Smit, H. (2001). *New data acquisition system for microphone array measurements in wind tunnels*, in 7th AIAA/CEAS Aeroacoustics Conference and Exhibit, American Institute of Aeronautics and Astronautics.
- [10] Sinske, J., Govers, Y., Jelcic, G., Handoyo, V., Krüger, W. R., Böswald, M. (2018). HALO flight test with instrumented under-wing stores for aeroelastic and load measurements in the DLR project iLOADS. *CEAS Aeronautical Journal*, 9(1): pp. 207-218.
- [11] Guillaume, P., Verboven, P., Vanlanduit, S., Van der Auweraer, H. , Peeters, B. (2003). *A poly-reference implementation of the least squares complex frequency-domain estimator*. in International Modal Analysis Conference. Kissimmee, FL, USA.
- [12] Peeters, B. , De Roeck, G. (1999). REFERENCE-BASED STOCHASTIC SUBSPACE IDENTIFICATION FOR OUTPUT-ONLY MODAL ANALYSIS. *Mechanical Systems and Signal Processing*, 13(6): pp. 855-878.
- [13] van Overschee, P. , de Moor, B. L. R. (1996). *Subspace identification for linear systems: Theory - Implementation - Applications*. Boston: Kluwer Academic Publishers. xiv, 254 p.

COPYRIGHT STATEMENT

The authors confirm that they, and/or their company or organization, hold copyright on all of the original material included in this paper. The authors also confirm that they have obtained permission, from the copyright holder of any third party material included in this paper, to publish it as part of their paper. The authors confirm that they give permission, or have obtained permission from the copyright holder of this paper, for the publication and distribution of this paper as part of the IFASD-2019 proceedings or as individual off-prints from the proceedings.